Available online at www.sciencedirect.com
ScienceDirect
Journal of Power Sources 173 (2007) 222–232
JOURNAL OF POWER SOURCES
www.elsevier.com/locate/jpowsour

Channel and rib geometric scale effects of flowfield plates on the performance and transient thermal behavior of a micro-PEM fuel cell

Shou-Shing Hsieh *, Kuan-Ming Chu

Department of Mechanical and Electro-Mechanical Engineering, National Sun Yat-Sen University, Kaohsiung, Taiwan 80424, ROC

Received 5 July 2007; received in revised form 1 August 2007; accepted 1 August 2007
Available online 7 August 2007

Abstract

Effects of channel and rib widths with an aspect ratio (*H*/*W*) of 0.67 of rectangular cross-sections flowfield plates on cell performance in terms of *VI*/*PI* curves versus flowfield pressure drop of a micro-proton exchange membrane (PEM) fuel cell were extensively examined. The channel-to-rib width ratios of flowfield plates were varied from 0.5 to 2. It was found that a channel-to-rib width ratio of unity was secured as far as the best performance of the *VI*/*PI* curves are concerned. Moreover, the pressure drop in flowfield on both anode and cathode was also measured. With the aid of pressure drop obtained for H_2/air delivery, an optimal channel-to-rib width ratio in terms of the net power gain factor (=power gain/power consumption) of 0.67 can be obtained for the cases under study. Furthermore, a simple lumped capacitance model was used to predict the temperature evolution of the fuel cell system, and results show that this model performs quite well, and the channel-to-rib width ratio seems no significant influence on the fuel cell temperature evolution of the flowfield plates.

Keywords: Channel-to-rib width ratio; Flowfield pressure drop; Micro-PEM fuel cells

1. Introduction

Proton exchange membrane (PEM) fuel cell has many advantages [1–3] compared with other types of fuel cells as portable power for mobility. The application of fuel cells to portable power is motivated by numerous occasions such as 3C products. Further, the use of micro-fabrication technology for fulfillment of power generation has ever been increased with being widely and generally demanded in portable electronic applications especially for 3C products. One of the notable and promising examples is micro-fuel cell system, for instance, micro-PEM fuel cell/micro-direct methanol (DM) fuel cell, which is now target for battery replacement for portable electronic devices and miniature power source. In general, the fuel cells produce between 30 mW (single cell) and 500 mW (cell stack) of power [4–6]. In fact, micro-fuel cells are expected to attain higher energy density than that of a lithium ion battery by converting hydrocarbon fuel to electric power at several percentage or higher efficiency.

A miniaturized fuel cell power source can be considered as an approach that combines thin film materials with micro-electromechanical system (MEMS) technology. Micro-fuel cells as mentioned before, which generate less than 5 W electricity for a single cell are generally developed either by silicon or polymeric micro-machinery with current collectors normally embedded in the flow channels [4,5,7]. Generally, fuel cell performance would increase as the channel gas flow velocity increases. However, an increase in gas velocity would facilitate reactant delivery to reaction sites by improved convective mass transport in a narrower flow channel.

It is known that the flowfield design influences not only the cell resistance but the mass transport of reactant gases and liquids. For a conventional PEM fuel cell, the main goals of flowfield design are to increase the uniformity of the current and temperature distribution at the operating conditions of interest while keeping or improving the cell performance. Studies of different flow patterns will give a concept of how to optimize the flowfield design for a PEM fuel cell stack [8]. This optimization would be obviously changed with the cell operating conditions.

One disadvantage of such a smaller size is the increased pressure drop in the flow channels. Flowfield configuration seems to greatly affect both the gas diffusion and electric conduction.

* Corresponding author. Tel.: +886 7 5252000x4215; fax: +886 7 5254215.
E-mail address: sshsieh@faculty.nsysu.edu.tw (S.-S. Hsieh).

0378-7753/$ – see front matter © 2007 Elsevier B.V. All rights reserved.
doi:10.1016/j.jpowsour.2007.08.005

Table 1
Geometry of the flow fields

	Case				
	1	2	3	4	5
Channel width (μm)	300	300	300	300	300
Rib width (μm)	600	450	300	200	150
Channel length (mm)	160	160	205	250	250
Channel pass	4	4	5	6	6
Channel number	28	28	36	44	44
Channel-to-rib width ratio	0.50	0.67	1.00	1.50	2.00
Open ratio (%)	37.9	38.7	49.2	59.6	60.0
Channel depth (μm)			200		
Reynolds number (anode)			6.26		
Reynolds number (cathode)			229.03		
Knudsen number (anode)			4.97×10^{-4}		
Knudsen number (cathode)			2.60×10^{-4}		
Mach number (anode)			0.0021		
Mach number (cathode)			0.0402		

Quick gas diffusion favors wider channel (narrower rib) width of flow channels. However, for a higher electric conduction, a narrower channel (i.e., wider rib) of flowfield configuration is needed to achieve a higher electric conduction. Therefore, it is necessary to investigate the geometric parameters involved with flow channels such as the flow channel type, the channel-to-rib width ratio, the rib shape, and the diffusion layer thickness on cell performance and pressure drop in detail as well.

Although there are a plenty of papers dealt with PEM fuel cells, few papers have reported works on a micro-fuel cell flow configuration especially with an optimum channel-to-rib width ratio. Further, there seems to be that no open literature available to discuss the effect for both the cell performance and flowfield pressure drop simultaneously. In this paper, effects of channel-to-rib width (with a rectangular cross-section) ratio of the serpentine flowfield on cell performance and pressure drop will be studied. An optimum operating condition with a trade-off to channel-to-rib width ratio will be obtained.

In this paper, we will focus on five different 5 cm^2 flowfield patterns with various rib widths and a given channel size for 28-channel serpentine, 36-channel serpentine, and 44-channel serpentine flows as listed in Table 1. Basically, they have similar patterns with three different gas path lengths. They were so designed that the effects of flow pattern and the path length on the cell performance and pressure drop can be examined simultaneously to provide and develop the generic design information for flowfields, which might be beneficial to the fuel cell industry especially for micro-fuel cell manufacturers. In addition, the fuel cell surface transient temperature distribution was also examined and discussed using the lumped capacity method. This study is a part of our main research goal of design and fabrication of a high performance micro-PEM fuel cell stack.

2. Experimental

2.1. Sample (including flow channels) preparation

In the present study, one of the most frequently used in commercial market flow channels, serpentine flow type channel with varying rib widths was micro-fabricated. Fig. 1 shows five different flowfields were used in the present experiments with rib width of 150, 250, 300, 450, and 600 μm with a definite channel width (300 μm). The resulting channel-to-rib width ratio is listed in Table 1 with relevant geometric variables of the channel. Following Hsieh et al. [9], the flowfield plates were fabricated with copper metal sheets by using LIGA-like (LIGA; a German acronym for lithographie galvanoformung abformung) micro-fabrication process of deep ultraviolet (UV) lithography to obtain SU-8 (2100) resist patterns/and SU-8 mould [9]. Fig. 2 shows the brief fabrication steps with proper parameters as listed in Table 2. Fig. 3(a)–(e) shows the images of a scanning examination microscope (SEM) and an atomic force microscope (AFM) examination, respectively. All samples had an active area of 2.25 cm long and 2.25 cm wide (5 cm^2). The flow channel was 2.25 cm long. The membrane electrode assembly (MEA) consisted of a Nafion 117 (ElectroChem) in combination with a platinum loading (Lynntech) of 1 and 0.5 mg/cm^2 on cathode and anode, respectively. Two 290 μm carbon papers (ELAT) from E-TEK served as the gas diffusion layers (GDLs) and were added to MEA. A single MEA was used for all five samples, minimizing the discrepancy in activation and ohmic losses between the testing of samples.

2.2. Single fuel cell and H_2/air circulating loop

The computer controlled single fuel cell system and circulating loop is designed (see Fig. 4 for details) for operation with hydrogen and air. The reactant gases are fed in series to the cells. Hydrogen (H_2) and air are conducted parallel-flow mode by varying channel/pass (serpentine) as also listed in Table 1 on both the anode and cathode of the single cell.

Purified (99.9%) and dry hydrogen is fed into the cell from a gas cylinder through a mass flow meter and back-pressure valve and compressed air was provided. The inlet flow rate of dry H_2 and air were regulated at 10 and 50 sccm, respectively, under different back pressures of 97, 153, and 207 kPa. These param-

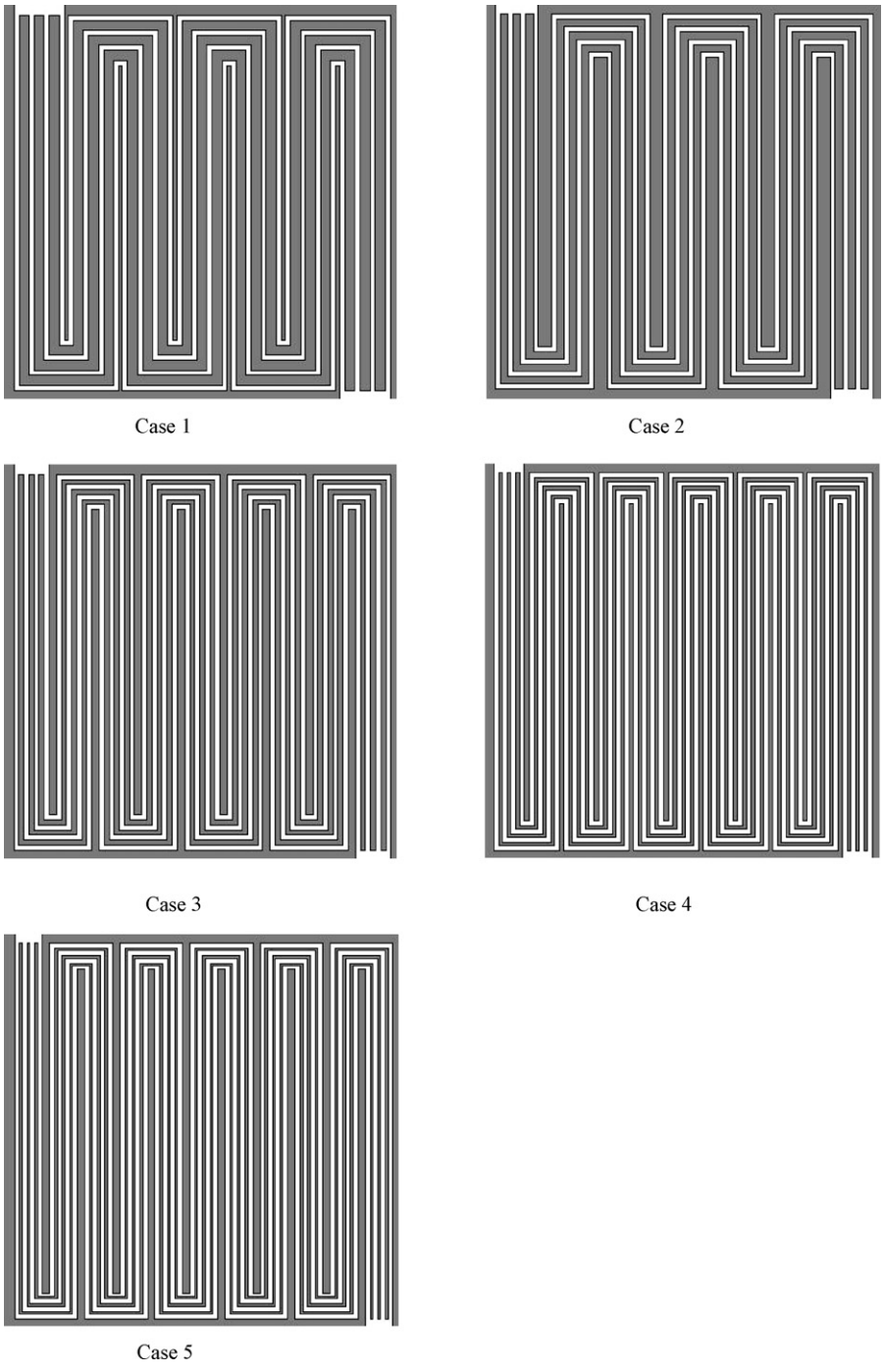

Fig. 1. Designs of the anode/cathode flow field.

eters also listed in Table 2 were controlled by a microprocessor based temperature controller and two back-pressure regulators. Current density versus voltage curves of the single cell were taken using a Gamry 4/750 potentiostat (scanning period 10 min) interfaced to a personal computer (PC) at constant current and recorded after the system reached a stable steady state (about 1 h) under the different operating conditions at a reasonable current density. The single cell surface temperature evolution was measured by a Testo 845 (Testo AG, Germany) infrared detector (IR) within ±0.1 °C accuracy.

2.3. Experimental conditions, system control, and data acquisition

The fuel cell system used was similar to that of Hsieh et al. [10] with slight modification for the single cell, which controls air and hydrogen flow rates, cell temperature, hydrogen/air back pressure, and current draw. The stand includes a potentiostat system (Gamry, PC4/750) for fuel cell operation and data acquisition. Tests with respect to performance and lifetime of the single cell are in progress. The single cell was operated at

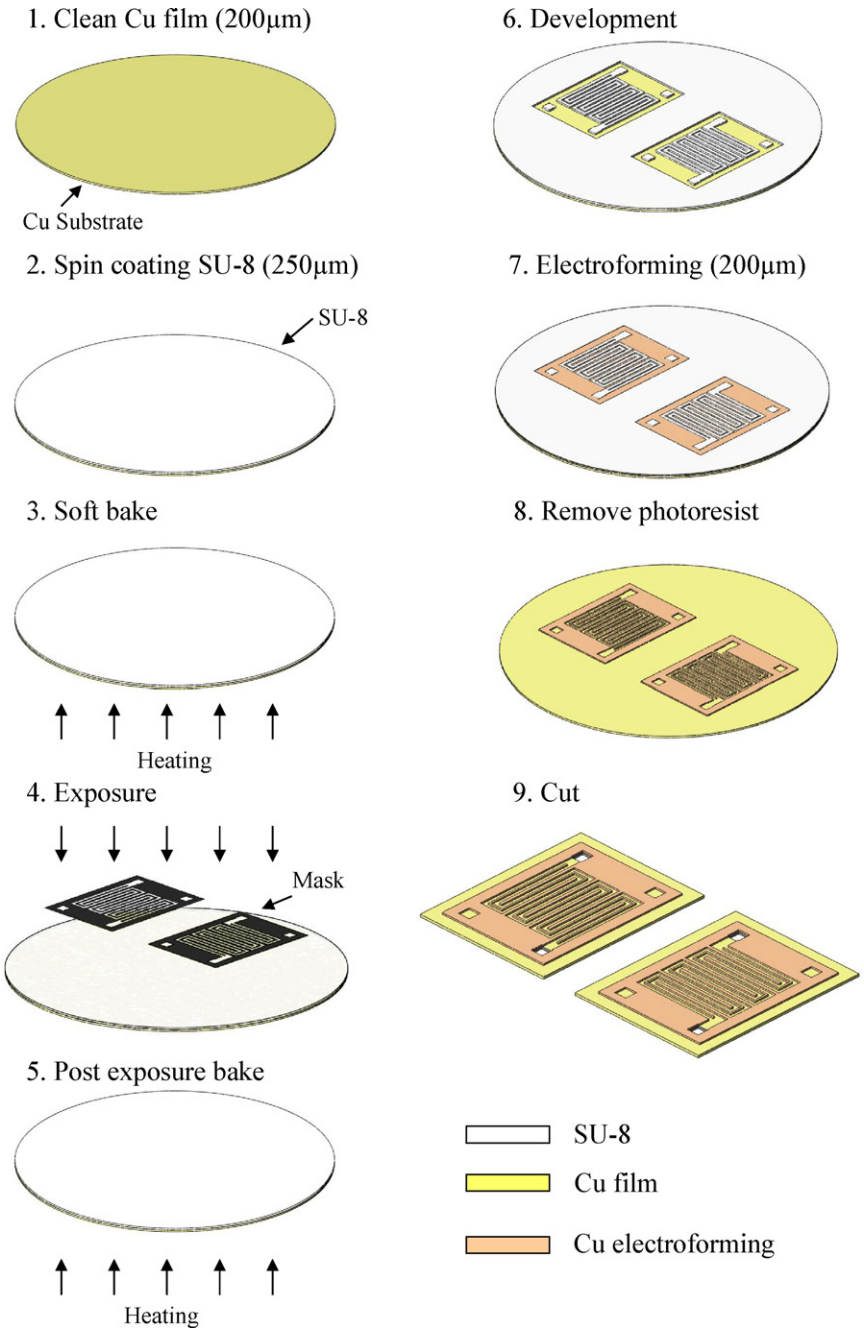

Fig. 2. Micro-fabrication processes of the fields plate.

25 °C. Since copper (Cu) sheet was used as flow plates material [11], durability as well as reliability examination was conducted for long-range tests (>60 days and each run with at least 5 h duration). The observation was shown in Fig. 5 and no noticeable difference (i.e., no clear voltage/power drop) as well as insignificant corrosion damage during the period of tests as shown in Fig. 5(a) and (b), respectively. This strongly suggests that copper sheets can be considered as one of possible candidates for flowfields material. In fact, copper metals enjoy higher mechanical strengths, better durability to shocks and vibration, no permeability, and much superior manufacturability and cost effectiveness when compared to carbon-based materials [10]. Therefore, copper sheets were used in this study. All fluid properties were calculated based on the ambient temperature of 298 K. This work was performed in University Microsystem Laboratory, National Sun Yat-Sen University.

3. Results and discussion

3.1. Reliability and durability examination

As stated previously, the single cell performance was tested for long-range runs (>2 months) and each test lasts at least 5 h. The *VI*/*PI* curves for all five different cases were examined as

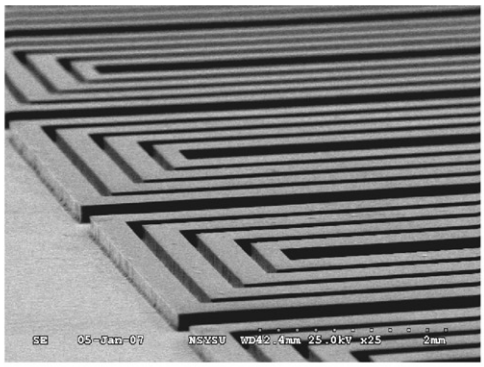

(a) SEM image of SU-8 pattern structure

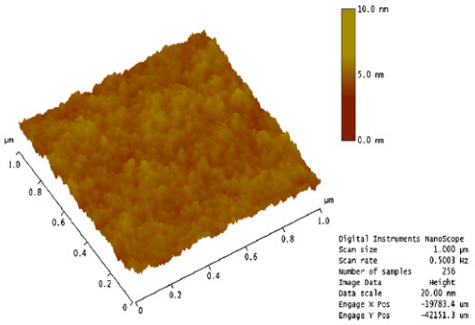

(b) 3-D AFM image of SU-8 pattern

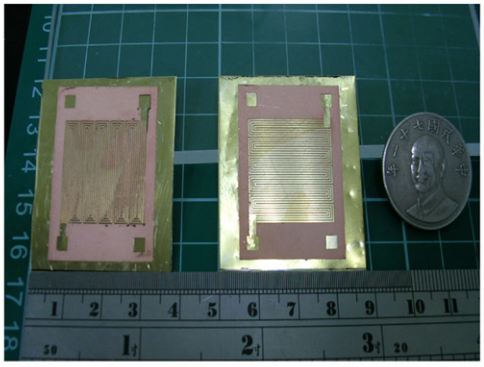

(c) Image of flow filed plate configuration

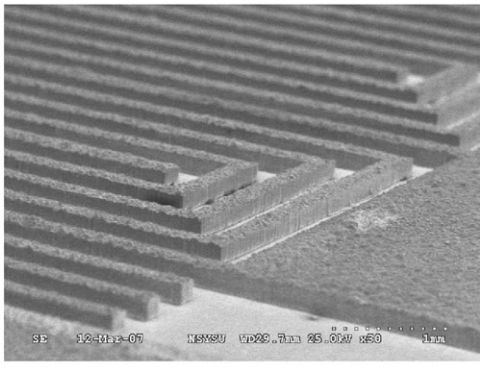

(d) SEM image of electroforming flow filed plate

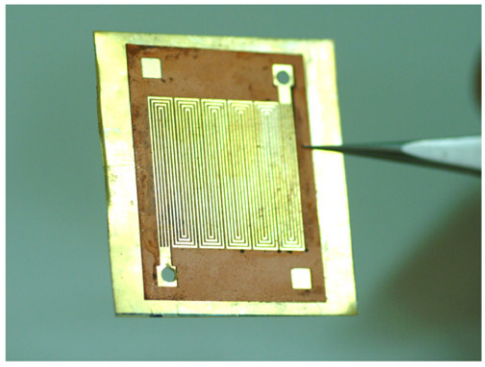

(e) Three-dimensional image of electroforming flow filed plate

Fig. 3. Images of flowfield plate configuration.

shown in Fig. 5(a). Fig. 5(b) shows open circuit voltage (OCV) profiles history for 5 h and it clearly suggests that the present copper sheet flowfield plates perform very well as far as the reliability and durability are concerned, which suggests the copper corrosion rate appears of no significance. Further inspection of this behavior can be done via an SEM examination of the used flowfield plates after 2 months as shown in Fig. 5(c). Basically, the used channel surface became more flat than that of the initial surface condition, due to the deposits filling into some small cavities on the surface of the originals as shown in Fig. 5(c); while for the rib surface, the growth of the oxide layer can clearly be noted and the growth rate was found to be about 0.06 μm/h. Based on the observation, one can conclude that the corrosion problems of copper metal flowfield plates can be considered negligible. In fact, we found that water flooding in reactant gas channels may occur and becomes more severe as time goes on. Further study is essentially needed for water disposal or recycle and related issues.

3.2. Channel-to-rib width ratio on flowfield pressure drop

Fig. 6(a)–(c) represent the pressure drop across anode/cathode flowfield and peak power density as function of channel-to-rib width ratio, channel open ratio, and

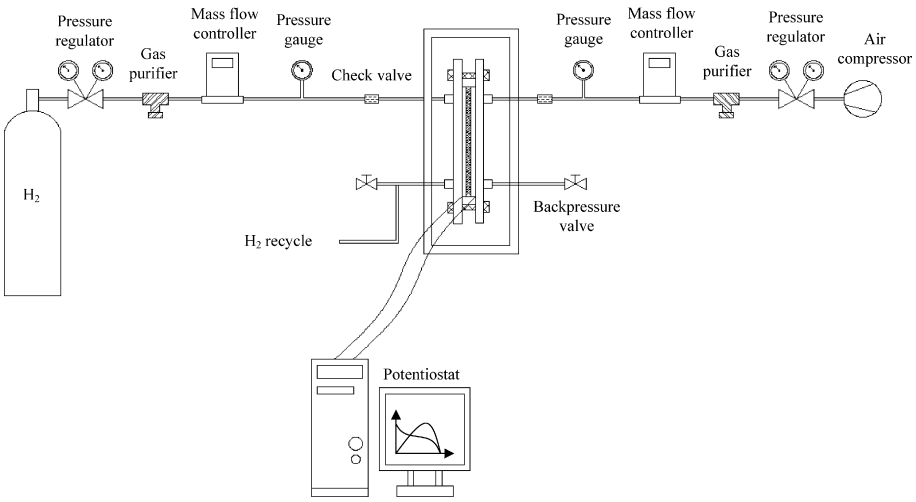

Fig. 4. Schematic of experimental apparatus for the present single cell.

channel length, respectively. Generally, in Fig. 6(a), starting from channel-to-rib width ratio 0.5 with ΔP of 25 kPa, the pressure drop in cathode flow channel are gradually increased until the channel-to-rib width ratio equals 1.5 and then gradually dropped and leveled off at about $\Delta P = 38$ kPa for channel-to-width ratio of 2. The increment of ΔP is considerable (about 13 kPa) with the channel-to-rib width ratio from 0.5 to 2; however, this situation becomes drastically small on anode. In fact, Fig. 6(a) also shows a nearly monotonic increase of ΔP from 3 to 5 kPa with the channel-to-rib width ratio from 0.5 to 2. This change is very small (<2 kPa). Also shown in Fig. 6(a) is peak power density distribution with various channel-to-rib width ratios and it is also found that a nearly constant peak power density prevails (≈48–50 mW/cm^2) for the channel-to-rib width ratio from 0.5 to 2.

Similarly, the channel open ratio effect can be noted in Fig. 6(b). Again, the curves shown indicate that the effect of channel open ratio on ΔP on cathode is very large as compared to that at anode; however, for peak power density, there seems no significance between these two electrodes again. Furthermore,

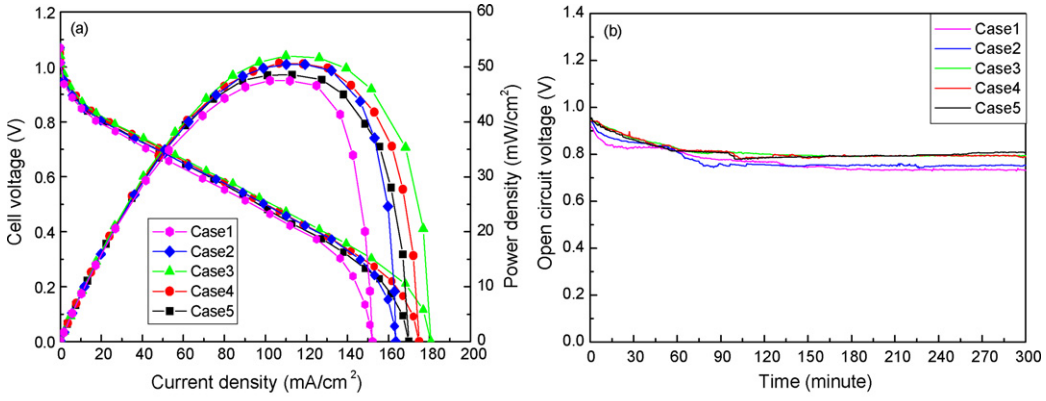

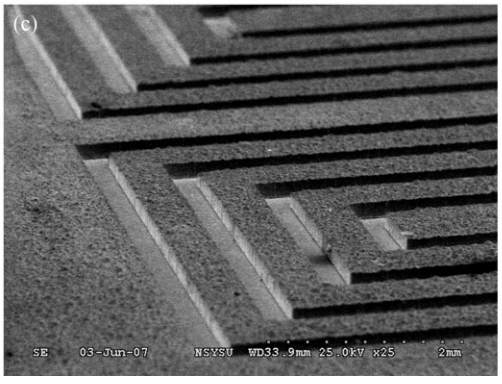

Fig. 5. (a) The long-term performance (5 h per day for 2 months); (b) durability test of single cell, for different cases at $T_{cell} = 25\,^{\circ}C$ and $P_{anode} = P_{cathode} = 97$ kPa; (c) electroforming flowfield plate after operating for 2 months.

Table 2
Fabrication parameters and conditions/experiment operating parameters

Fabrication parameters and conditions			
PR coating	SU-8 2100		
PR property	Negative		
PR type	Thick film		
Dehydration bake (°C)	150		
Speed (rpm)	400 (40 s); 700 (60 s)		
Soft bake (95 °C) (min)	150		
UV light wave length (nm)	365		
Light intensity (mW/cm^2)	17		
Exposure time (s)	65		
Post-exposure bake (95 °C) (min)	17		
Development (min)	3		
Electroforming solution	Copper sulfate, H_2SO_4 solution		
Solution pH	4		
Solution temperature (°C)	40		
Current density (mA/cm^2)	10		
Photoresist remover	Remover propylene glycol		
Experiment operating parameters			
Inlet gas			
Anode	Hydrogen (99.9%)		
Cathode	Air		
Flow rate			
Anode	10 sccm		
Cathode	50 sccm		
Gas backpressure			
Anode	97 kPa	153 kPa	207 kPa
Cathode	97 kPa	153 kPa	207 kPa
Cell temperature	25 °C	35 °C	50 °C
MEAs			
Nafion 117			
Anode	Pt on carbon (0.5 mg/cm^2)		
Cathode	Pt on carbon (0.5 mg/cm^2)		
GDL			
Anode	Carbon paper based material (290 μm)		
Cathode	Carbon paper based material (290 μm)		
Electrode	Copper		
Active area	5 cm^2		
Cell numbers	Single cell		

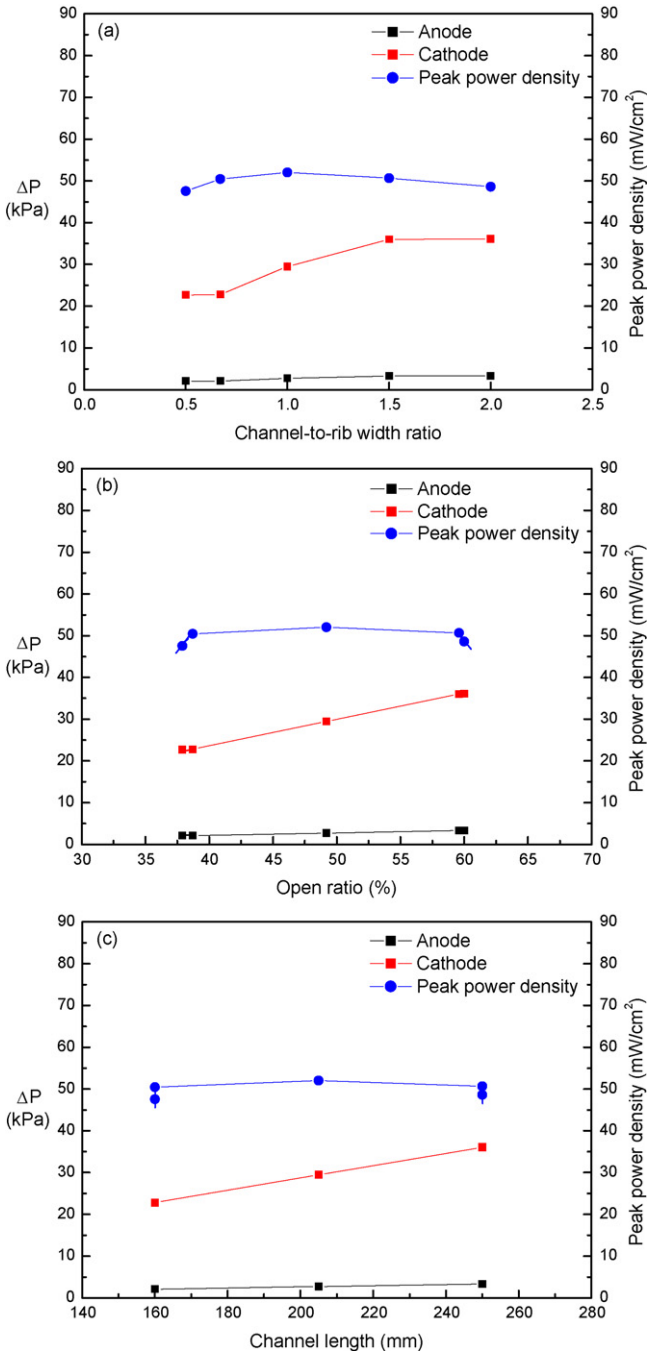

Fig. 6. The effects of channel-to-rib width ratio, open ratio, and channel length on the peak power density and the pressure drop (ΔP) at $T_{cell} = 25\,°C$ and $P_{anode} = P_{cathode} = 97$ kPa.

as depicted in Fig. 6(c), the channel length effect on cathode is much higher than that on anode as Fig. 6(a) and (b) show, possibly due to a much higher flow rate in cathode flow channel.

Fig. 7(a) and (b) represent pressure drop (ΔP) distribution across anode/cathode flow channel versus anode/cathode inlet back pressure for all the cases studied herein, respectively. Generally, a monotonic increase as well as consistent trend with different ΔP drop was found as the anode/cathode inlet pressure increases. Unlike Fig. 7, Fig. 8 shows the cell operating temperature on ΔP for all five cases on anode/cathode, respectively. As one can see, the influence appears quite small and it can be considered to be negligible as cell operating temperatures from 25 to 50 °C especially on the cathode.

Based on examination on the pressure drop across the anode/cathode flow channel as well as the corresponding performance characteristics (e.g., *VI*/*PI* curves), one optimum case, like case 3, of which an open ratio of 0.5 and a channel-to-rib width ratio of unity was found. Consequently, *VI*/*PI* curves were thus plotted at the cell operating temperature of 25 °C with various inlet anode/cathode back pressure of 97, 153, and 207 kPa. Fig. 9(a) shows the same inlet back pressure on both anode/cathode flow channel; while, Fig. 9(b) shows the results of the mixed inlet pressure condition. It is seen although the inlet back pressure on anode/cathode is different, the performance in terms of *VI*/*PI* curves shows its superiority especially for $P_{cathode} > P_{anode}$ as illustrated in Fig. 9(b).

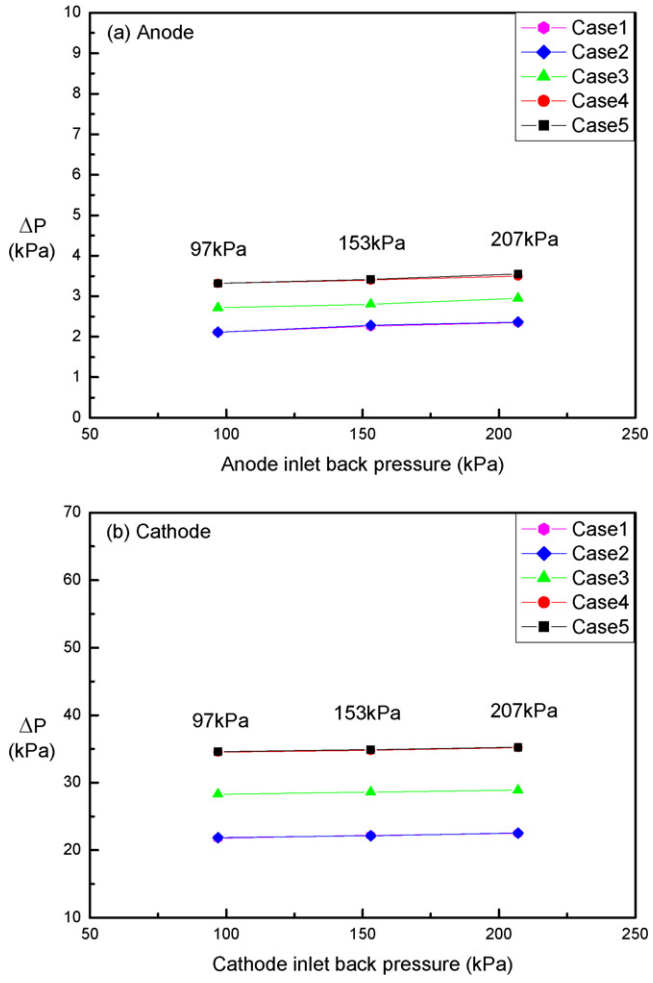

Fig. 7. Channel pressure drop with different inlet anode and cathode back pressure at $T_{cell} = 25\,^{\circ}C$.

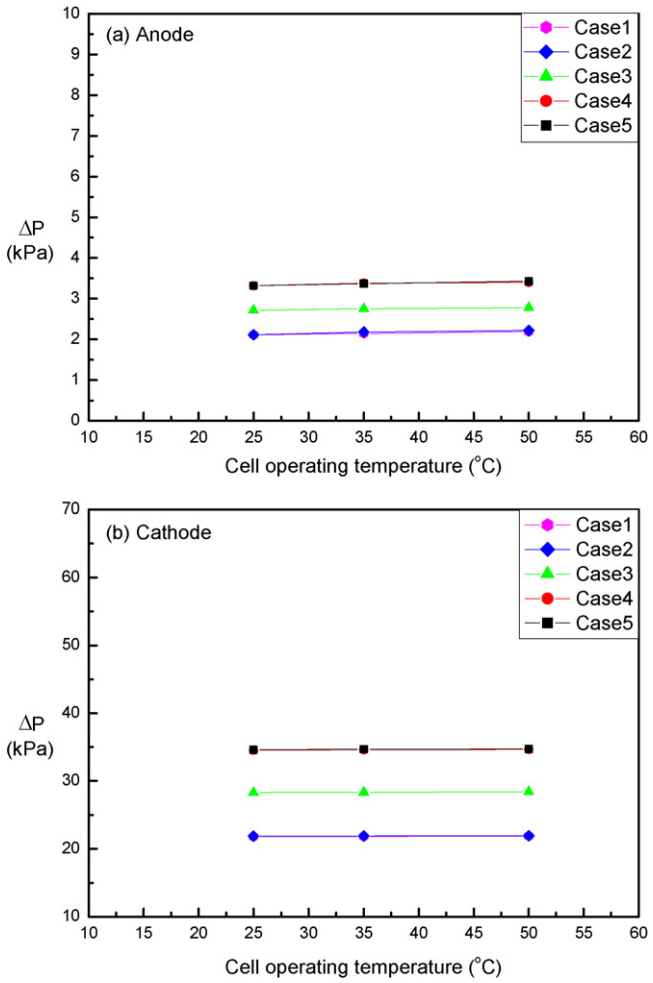

Fig. 8. ΔP vs. cell operating temperature at a fixed $P_{anode} = P_{cathode} = 97$ kPa.

3.3. Channel-to-rib width ratio on VI/PI curves

Fig. 10 exhibits a performance test expressed by *VI/PI* curves with different operating temperatures of 25, 35, and 50 °C at a fixed $P_{anode} = P_{cathode} = 97$ kPa. As expected, the OCV (to 1.15 V)/limiting current density (to 220 mA/cm^2) would increase as the cell operating temperature increase for case 3. In order to enhance and broaden our fundamental understanding, limiting current density as well as peak power density were plotted against the channel-to-rib width ratio, respectively, at $T_{cell} = 25\,^{\circ}C$, $P_{anode} = P_{cathode} = 97$ kPa, and the results are thus shown in Fig. 11. Again, the ratio of unity presents the best performance on both limiting current density (≈180 mA/cm^2) and peak power density (50 mW/cm^2), of which these values can also be read out from Fig. 10, for instance.

It is known that the dimensions of the channels and their spacing affect the reactant gas (H_2/or air) access to the gas diffusion layer and also provide wide area for water removal from the gas diffusion layer. This would result in an increase in proton conductivity. However, this could also cause a poor electron transfer due to a narrow spacing. On the contrary, wide spacing enhances conduction of electrical current and heat; however, it simultaneously reduces the area directly exposed to the reactants and promotes the accumulation of water. Consequently, it results in a poor cell performance. Based on the aforementioned two counteracting factors, an optimum channel-to-rib width ratio of unity was found like case 3. Further, with the effect of channel pressure drop also considered, this ratio would be changed and becomes less than unity. In fact, it was found to be 0.67 in the present study.

3.4. Optimal channel-to-rib width ratio versus VI/PI curves and pressure drop

Fig. 12 further extracted the previous results of pressure drop to obtain the friction factor for all five cases under study. The friction factor calculation was based on the known Darcy–Weisbach formula and the data on both anode/cathode flow channel was plotted as shown in Fig. 12(a) and (b), respectively, against the channel-to-rib width ratio at $T_{cell} = 25\,^{\circ}C$ and $P_{anode} = P_{cathode} = 97$ kPa. It is found that the friction factor value nearly constant on each flow channel; it is about 9.8–9.9 on anode; while on cathode is about 0.28–0.29. Also included in Fig. 12 are the pressure drop distribution on anode/cathode for reference. Since the present flow condition is still in continuum

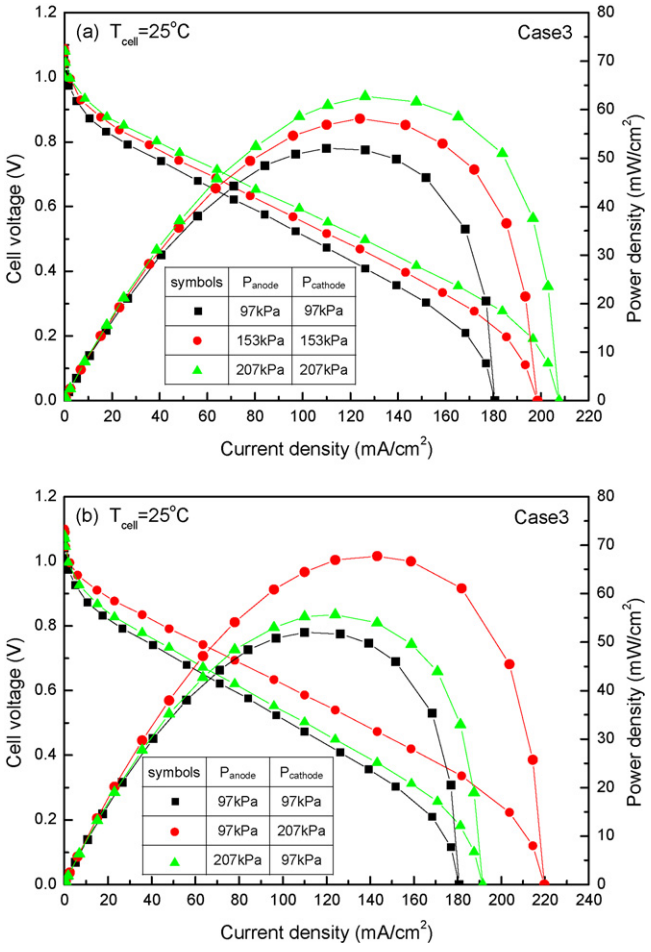

Fig. 9. The performance test for single cell with an optimum condition. (a) Different operating pressure of the anode and the cathode side; (b) pressurized anode and pressurized cathode sides.

flow region (i.e., $Kn \approx 0$, see Table 1 for details), the friction factor obtained can be compared with those conventional empirical friction factor (f) formula ($f = 60.4/Re$) for laminar flow with the same Reynolds number. It is found that the deviation is very small (<8%), which again, strongly suggests and also verifies

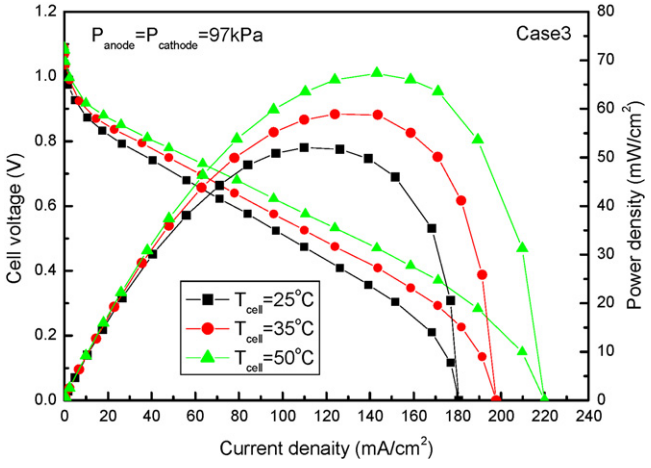

Fig. 10. The performance test for single cell at different cell temperature with an optimum condition.

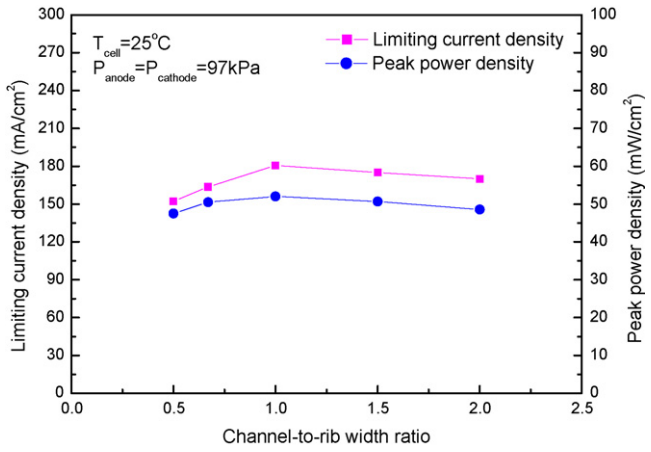

Fig. 11. The peak power density and the limiting current density vs. channel-to-rib width ratio.

the validity of the present pressure drop measurements for both anode/cathode flow channel.

Furthermore, based on the pressure drop across the anode (~2 kPa) and cathode (~30 kPa), it can be seen that the pressure drop (ΔP) is about on the order of one-hundreds of a bar or a fraction of one-hundreds of a bar. Regardless of how the pressure difference is obtained in either anode or cathode

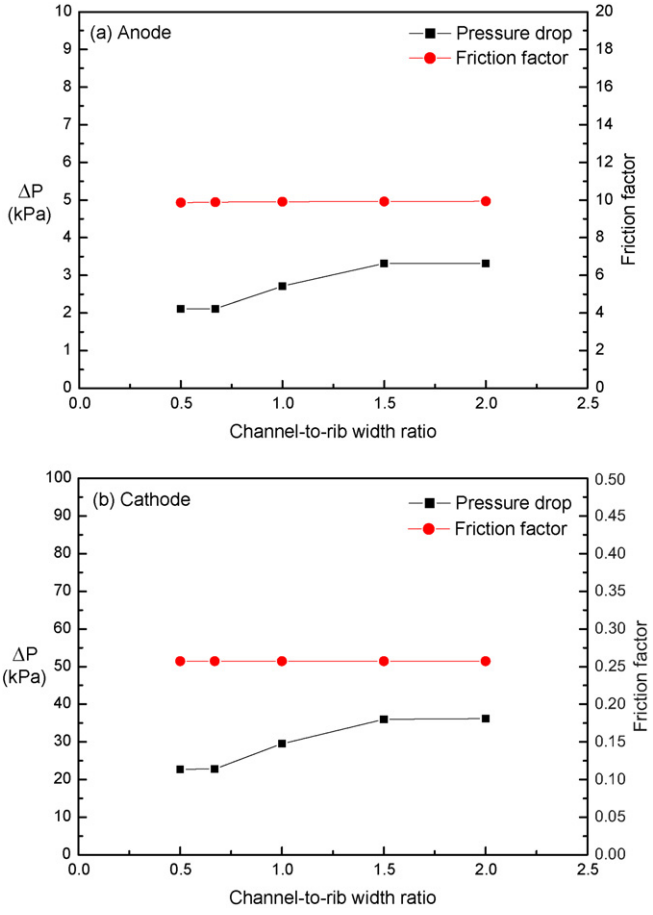

Fig. 12. The pressure drop (ΔP) and the friction factor vs. the channel-to-rib width ratio at $T_{cell} = 25\,^{\circ}C$ and $P_{anode} = P_{cathode} = 97$ kPa.

channel, the value is comparable to that of nonmicrosystems and it can be considered a constant. With this assumption, the velocity scale (U) in anode/or cathode microchannel is proportional to the length scale (say ℓ); i.e., $U \sim \ell$. Since $Re = U\ell/\nu$, $Re \sim \ell^2$. According to the Darcy–Weisbach equation, the friction factor (f) is portional to ℓ^{-2} with a constant ΔP. Therefore, $f \sim Re^{-1}$. This functional relationship is again valid in the present anode/cathode microchannels when the flow is laminar, which is also evidenced by the present experimental results, as stated previously.

3.5. Cell surface temperature evolution

Furthermore, transient temperature history for five cases were also presented in Fig. 13(a) and (b), respectively on both anode/cathode flow channel and polymethyl methacrylate (PMMA) surface (single cell housing) via an IR detector (pointwise measurements) with a resolution of ±0.1 °C and the results were plotted against time for the first 300 min. The temperature history seems not to be varied significantly on the anode and consistent with the cell operating temperature (≈24.6 °C); while, on the cathode, there is a temperature increases as compared to the cell temperature (25 °C) to a peak and, thereafter, it reaches its plateau having a constant temperature difference (∼4 °C) with the ambient until 15 min elapsed. This is evident because the exothermic reaction occurs on the cathode. Also shown in Fig. 13(b) is the inset of the initial 30 min, which was enlarged for clarity. One can clearly see the temperature deviations for five cases under study. But, they all would be leveled off after 30 min, and the steady state would be reached thereafter.

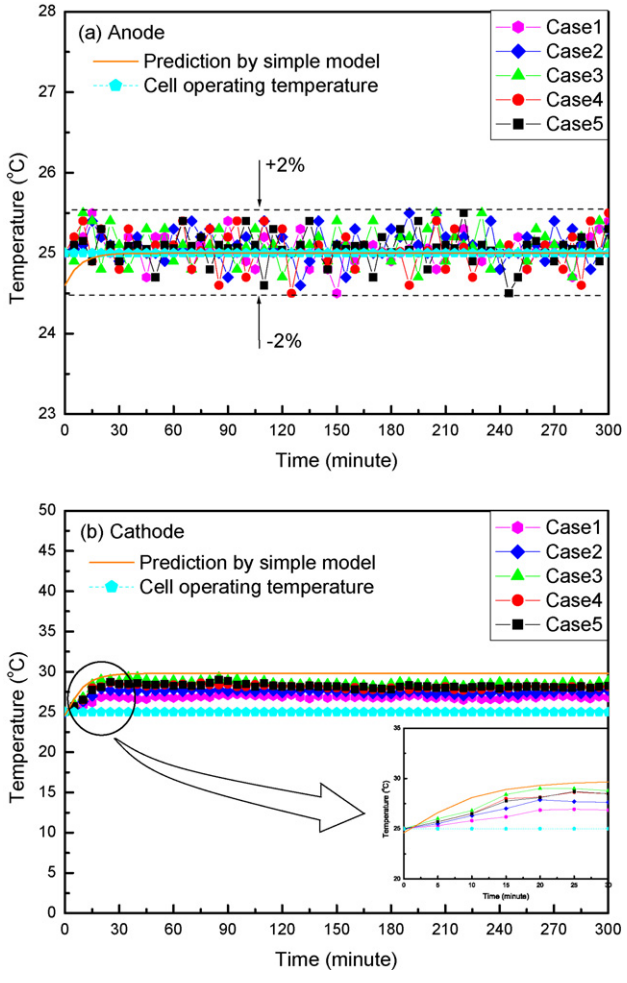

Fig. 13. Comparisons of the present temperature measurements on anode/cathode surface with those from prediction.

On the cathode, while exothermic reactions occur, we thus have an input of chemical energy (Q_g) per unit time, which is

$$Q_g \sim \ell^3$$

The micro-fuel cell transfers heat towards the ambient through microchannel with a thickness of δ and surface area S. The amount of heat released (Q_0) per unit time via fuel cell is thus

$$Q_0 = \frac{kS}{\delta}\Delta T$$

where k is the thermal conductivity of the micro-fuel cell and ΔT is the temperature difference between the micro-fuel cell and ambient. Since surface area S and the thickness of the micro-fuel cell δ are proportional to ℓ^2 and ℓ, respectively. We obtain

$$Q_0 \sim \ell$$

which indicates that the heat transferred to the ambient is much more than the fuel cell generated. Consequently, the anode surface and cathode surface would be cooled down to the ambient temperature or so very quickly as also can be assessed in Fig. 13. Note that the present micro-fuel cell system consisted of three composite layer of MEA (only one half was considered due to symmetry), flow channel, and PMMA plate.

The temperature history from the simple lumped capacitance model can be found to have the following form on the cathode and anode, respectively:

$$\text{(cathode)}\quad T - T_\infty = \left(\frac{T_0 - T_\infty - q'''V}{hA}\right) e^{-(\mathrm{BiFo})} + \left(\frac{q'''V}{hA}\right),$$

$$\text{(anode)}\quad T - T_\infty = (T_0 - T_\infty)\, e^{-(\mathrm{BiFo})}$$

where T_∞ is the ambient temperature, $\mathrm{Bi} = hL/k$ with h the convective heat transfer coefficient, k the effective thermal conductivity of the three composite layers, and L is the thickness of three composite layers, $\mathrm{Fo} = \alpha t/L^2$; here α is the thermal diffusivity of the composite materials, t is time, and V and A are the volume and cross-section composite layers, respectively. q''' is volumetric heat generation and can be obtained from the exothermic reaction on the cathode (i.e., $q''' = 0$ on the anode).

These results were also included in Fig. 13(a) and (b) for comparison on both anode and cathode, respectively. In fact, based on a lumped capacitance model (Biot number $O(10^{-2}) < 0.1$ in the present study while copper metal was used as a flowfield plate with both the effect of MEA and PMMA thermal conductivity also included), the time constant (τ) can be estimated (≈191 s) for case 3. After five times time constant (i.e., $t \geq 5\tau$, say) elapsed, the steady state temperature of 29.3 °C can be found,

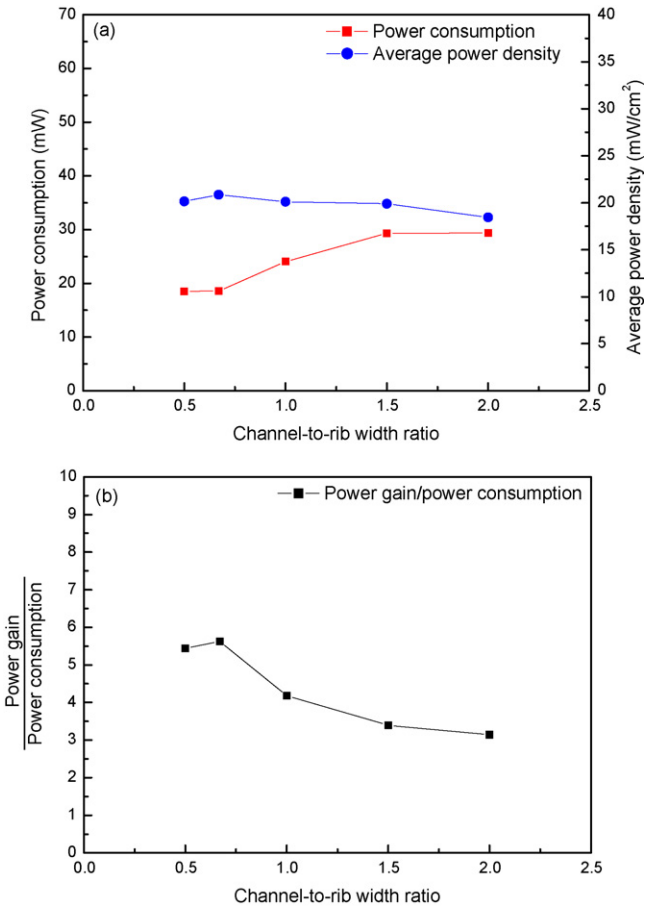

Fig. 14. (a) Power consumption and average power density; (b) power gain/power consumption, vs. channel-to-rib width ratio at $T_{cell} = 25\,^{\circ}C$ and $P_{anode} = P_{cathode} = 97$ kPa.

which is very close to the steady state (about 1050 s) results (≈29.1 °C) from the IR detector pointwise measurements with the deviation less than ±1%. These two values of time duration for reaching a steady state are quietly close within a derivation less than ±9%. This strongly indicates that the present simplified model used to simulate the present micro-fuel is appropriate and seems promising, and can further be applied to the related fuel cell systems. Naturally, the time history of the temperature distribution for case 3 would be a little bit higher than those of other cases due to a superior performance. But this difference seems of no significance.

Fig. 14(a) depicts the power consumption calculated based the pressure drop measurements via the equation of $(\dot{m}\Delta P)/\rho$ due to the fuel H_2/air delivery on the anode and cathode and the average power density distribution (power gain) measured are the function of channel-to-rib ratio, respectively, for the case of $T_{cell} = 25\,^{\circ}C$ and $P_{anode} = P_{cathode} = 97$ kPa. While, Fig. 14(b) shows the net power gain factor defined as the ratio of power gain to power consumption. The net power gain factor was found in the range of 3–6 and it can reach up to a maximum value of about 6 at channel-to-rib width ratio of 0.67, which is different from the one of channel-to-rib ratios of unity for considering the best *VI*/*PI* curves.

4. Conclusions

The channel and rib geometric scale effects of flowfield plates on the performance of a micro-PEM fuel cell were examined and discussed. Through *VI*/*PI* curves and the anode and cathode flowfield pressure drop measurements, an optimum channel-to-rib width ratio in the range of the present study of 0.5–2 was found to be 0.67 as far as the net power gain (power gain/power consumption) was concerned. While, if only *VI*/*PI* performance curves considered, the above-stated value would become a little bit bigger, and it was found to be 1. In addition, using a simple lumped capacitance model for heat transport, the temperature distributions on the cathode surface can easily be predicated and found to be in good agreement with those of IR detector (pointwise) measurements. Channel and rib geometric scale effect on the cell system transient temperature distribution seems of no significance. Moreover, a long-range and reliability test was also conducted for the present micro-PEM single fuel cell using copper metal as flowfield materials via a consecutive 5 h operation every day for 2 months. It is found that the copper corrosion rate is not significant and the fuel cell operates quite stable as far as both *VI*/*PI* polarization characteristics are concerned.

References

[1] P. Krishnan, J.S. Park, T.H. Yang, W.W. Lee, C.S. Kim, J. Power Sources 163 (2006) 2–8.
[2] K. Tüber, A. Oedegaard, M. Hermann, C. Hebling, J. Power Sources 131 (2004) 175–181.
[3] S. Kim, S. Shimpalee, J.W.V. Zee, J. Power Sources 135 (2004) 110–121.
[4] S.-S. Hsieh, J.K. Kuo, C.F. Hwang, H.H. Tsai, Microsyst. Technol. 10 (2004) 121–126.
[5] S.-S. Hsieh, C.F. Hwang, J.K. Kuo, H.H. Tsai, S.H. Yang, J. Solid State Electrochem. 9 (2005) 121–131.
[6] K.G. Stanley, E.K. Czyzewska, P.K. Vanderhoek, L.Y. Fan, K.A. Abel, Q.M. Wu, M. Parameswaran, J. Micromech. Microeng. 15 (2005) 1979–1987.
[7] S.H. Chan, N.T. Nguyen, Z. Xia, Z. Wu, J. Micromech. Microeng. 15 (2005) 231–236.
[8] S. Shimpalee, S. Greenway, J.W. Vanzee, J. Power Sources 160 (2006) 398–406.
[9] S.-S. Hsieh, C.F. Huang, C.L. Feng, Micron, in press.
[10] S.-S. Hsieh, C.L. Feng, C.F. Huang, J. Power Sources 163 (2006) 440–449.
[11] H. Tawfik, Y. Hung, D. Mahajan, J. Power Sources 163 (2007) 755–767.